Transverse revival and fractional revival of the Hanbury Brown and Twiss bunching effect with discrete chaotic light

Liming Li,[1] Peilong Hong,[2] and Guoquan Zhang[1,3,*]

[1]*The MOE Key Laboratory of Weak-Light Nonlinear Photonics, School of Physics and TEDA Applied Physics Institute, Nankai University, Tianjin 300457, China*

[2]*Faculty of Science, Ningbo University, Ningbo 315211, China*

[3]*Collaborative Innovation Center of Extreme Optics, Shanxi University, Taiyuan, Shanxi 030006, China*

(Received 21 September 2018; published 25 February 2019)

We studied the Hanbury Brown and Twiss (HBT) bunching effect of discrete chaotic light sources. It is found that, for periodical discrete chaotic light sources, the HBT bunching effect collapses first but then revives repeatedly at specific transverse distances between two detectors in the far-field detection plane, which is very different from the HBT bunching effect with a spatially continuous chaotic light source. Such transverse revivals of the HBT bunching effect are the result of in-phase superposition of all discrete two-photon eigen modes of the periodical discrete chaotic light sources. In addition to the integer HBT bunching revival, the fractional HBT bunching revival can also be observed with nonperiodical discrete chaotic light sources due to the in-phase constructive interference of parts of the two-photon eigen modes. Experimental verification on both the integer and the fractional HBT bunching revivals are given. The transverse revival and fractional revival of the HBT bunching effect provide an efficient way for imaging processing such as ghost image copy in the detection plane.

DOI: 10.1103/PhysRevA.99.023848

I. INTRODUCTION

Discrete systems are universal in nature, from microscopic elementary particles, atoms and molecules, mesoscopic nanoparticles and structures, and macroscopic periodical structures such as gratings and optical waveguide arrays, to even cosmoscopic objects, which are of very different physical properties from the continuous systems. Poincaré recurrence theorem indicates that systems with discrete eigen values will eventually return arbitrarily close to its initial state [1,2], which is generally called the revival effect of quantum wave packet [3] extensively studied in many bounded quantum systems such as the infinite well [4–6], the harmonic oscillators [7–9], the Rydberg atoms [10–12], the two-level atoms interacting with coherent fields [13–17], a collection of anharmonically confined atoms [18], and even the macroscopic Bose-Einstein condensates [19–22], just to mention a few. The underlying physics for the revival and fractional revival of the wave packets is the in-phase superposition of the discrete eigen wave functions of the bounded quantum systems after the collapse of the initial states due to the dephasing evolution among the discrete eigen wave functions [3,23]. The wave-packet revival is not only of fundamental importance to understand the correspondence principle which is at the heart of quantum mechanism but also of technical significance in the development of novel techniques to control or produce specific quantum states.

In optics, a large amount of revival effects were reported in various linear and nonlinear systems in both the spatial and frequency domains [24–31]. A typical revival effects in optics is the Talbot effect [24], which manifested itself as repeated self-imaging of the objects at certain regular distance, the so-called Talbot distance, in the longitudinal propagation dimension when light transmits through periodical structures such as gratings. Rayleigh first interpreted the Talbot effect as a consequence of the interference among spatially coherent diffracted light from the gratings [32]. Lau found that such self-imaging effect can also be observed even under incoherent illuminations [25]. Much attention has been paid to the Talbot effect and the development of related applications such as optical imaging processing, optical lithography, optical metrology and spectrometry [33–35]. New Talbot effects, such as discrete Talbot effect in waveguide arrays [27] and nonlinear Talbot effect with periodically poled lithium tantalate crystals [29], were also reported. The Talbot self-imaging technique can also be extended to various areas such as x-ray, electron microscopy, plasmonics, acoustics, and Bose-Einstein condensates [33,34].

One may note that all the above-mentioned revival and fractional revival effects are based on the first-order in-phase constructive interference. For optical fields, the second-order optical coherence was discovered by Hanbury Brown and Twiss (HBT), known as the HBT bunching effect of thermal light [36,37], and the second-order Talbot effect was proposed based on the second-order optical coherence and demonstrated experimentally with both entangled photon sources [28,38,39] and thermal light sources [40,41], respectively. The Talbot distance in the second-order optical coherence is found to be half of that in the classical first-order optical coherence, but the spatial resolution of the second-order Talbot self-imaging was not improved as compared to that in the traditional first-order Talbot self-imaging [35,39]. Note that the Talbot self-imaging, no matter in the first-order or the

*zhanggq@nankai.edu.cn

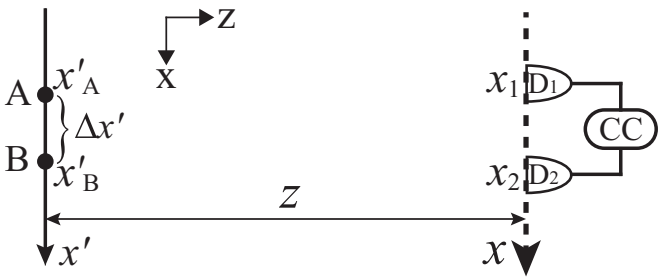

FIG. 1. Fundamental scheme to study the first- and second-order coherence between two independent chaotic point light sources A and B. D_1 and D_2: single-photon detectors. CC: coincidence counting system.

second-order optical coherence, are in the Fresnel diffraction configuration and repeated in the longitudinal propagation dimension [33,35]. Comprehensive reviews about the Talbot effect can be found in Refs. [33,35].

In this paper, we reported on the revival and the fractional revival of the HBT bunching effect with a discrete chaotic light source, which is a result of in-phase superposition of multiple discrete two-photon eigen modes. Different from the revival of wave packet in quantum systems or self-imaging of the object structure in the Talbot effect, here it is the HBT bunching effect of chaotic light that is revived. In addition, the HBT bunching effect is revived repeatedly in the transverse dimension instead of the traditional longitudinal dimension such as that in the Talbot effect. Possible applications on the imaging processing was also proposed and demonstrated.

II. THEORETICAL MODEL AND RESULTS

For simplicity but without loss of generality, here we will give a detailed analytical result about the transverse revival and fractional revival of the HBT bunching effect for the one-dimensional (1D) case; the extension to the two-dimensional (2D) case is direct and therefore will not describe here again. However, experimental verification for both the 1D and 2D cases will be provided in Secs. III and IV. In addition, for the chaotic light sources, we assume the light intensity is temporally stable while the phase changes randomly. Such chaotic light sources can be experimentally designed by using a spatial light modulator (SLM), as we will show in the experimental part Sec. III. In the following, the HBT effects of three different chaotic light sources, namely, two independent chaotic point light sources, continuous chaotic light sources and discrete chaotic point light sources, respectively, are studied analytically, exhibiting very different HBT bunching behaviors, respectively.

A. Two independent chaotic point light sources

The simplest case is the one for two independent chaotic point light sources, which has been well studied in the literature [36,37,42–48]. For comparison and completeness, here we give a brief description of the HBT behavior of the two independent chaotic point light sources, which is helpful to understand the results of the other two cases. Figure 1 shows the fundamental scheme to study the first- and second-order coherence effects between two spatially separated and completely independent chaotic point light sources A and B, where $D_i (i = 1, 2)$ is the single-photon detector placed on the far-field detection plane (or the Fraunhofer zone). The first-order coherence can be studied by using a single-photon detector to record the spatial distribution of the light intensity on the far-field detection plane, while the second-order coherence can be measured with two single-photon detectors and a photon coincidence counting system (CC in Fig. 1).

When the two point light sources are completely independent, it is evident that they are first-order incoherent, but one can observe the second-order interference fringes [46,47],

$$G^{(2)}(x_1, x_2) = \langle (|E_{\mathrm{O,A}}|^2 + |E_{\mathrm{O,B}}|^2)^2 \rangle + 2\langle |E_{\mathrm{O,A}}|^2 \rangle \langle |E_{\mathrm{O,B}}|^2 \rangle \cos(k\Delta x'(x_1 - x_2)/z), \quad (1)$$

where $\langle \cdots \rangle$ stands for the ensemble average, $E_{\mathrm{O,A}}$ and $E_{\mathrm{O,B}}$ are the instantaneous electric field amplitude on the detection plane but originating from the point light sources A and B, respectively, which satisfies $|E_{\mathrm{O,i}}| \propto \frac{1}{\lambda z}|E_{\mathrm{S,i}}|$, where λ and $E_{\mathrm{S,i}}$ are the wavelength and the instantaneous field amplitudes of sources $i = \mathrm{A}, \mathrm{B}$, respectively. $k = 2\pi/\lambda$ is the wave number of light, $\Delta x' = x'_{\mathrm{A}} - x'_{\mathrm{B}}$ is the displacement between two point light sources A and B on the source plane, with x'_{A} and x'_{B} being their respective positions, x_1 and x_2 are the positions of two single-photon detectors on the detection plane, and z is the distance between the detection plane and the source plane, respectively. Here, we consider only the scalar light field for simplicity.

It is evident that the second-order correlation function $G^{(2)}(x_1, x_2)$ consists of two contributions [42]: (1) the self-correlation part $G^{(2)}_{\mathrm{self}}(x_1, x_2)$ with the pair of detected photons from the same point light source which only contributes a constant background; (2) the cross-correlation part $G^{(2)}_{\mathrm{cross}}(x_1, x_2)$ with the pair of detected photons from two different sources which leads to the superposition of two different but indistinguishable two-photon paths, resulting in the two-photon interference fringes. Here, the second-order spatial cross-correlation function of the two independent chaotic point light sources can be expressed as [43–48]

$$\begin{aligned} G^{(2)}_{\mathrm{cross}}(x_1, x_2) &= 2\langle |E_{\mathrm{O,A}}|^2 \rangle \langle |E_{\mathrm{O,B}}|^2 \rangle [1 + \cos(k\Delta x'(x_1 - x_2)/z)] \\ &= 2I_0^2 \mathrm{Re}(1 + e^{-ik\Delta x'(x_1 - x_2)/z}), \end{aligned} \quad (2)$$

forming an oscillating two-photon eigen mode $e^{-ik\Delta x'(x_1 - x_2)/z}$ of the second-order interference fringes with a characteristic eigen spatial frequency $\Delta x'/(\lambda z)$ determined by the displacement $\Delta x'$ if the propagation distance z is fixed. Here, for simplicity, we set the two chaotic point sources of equal field amplitude and intensity; therefore, it satisfies $\langle |E_{\mathrm{O,A}}|^2 \rangle = \langle |E_{\mathrm{O,B}}|^2 \rangle = I_0$ on the detection plane. The symbol $\mathrm{Re}(\cdots)$ means to take the real part of the variable inside the bracket.

B. Continuous chaotic light sources

For a continuous chaotic light source with a spatial dimension of $[-R, R]$ and spatially homogeneous field

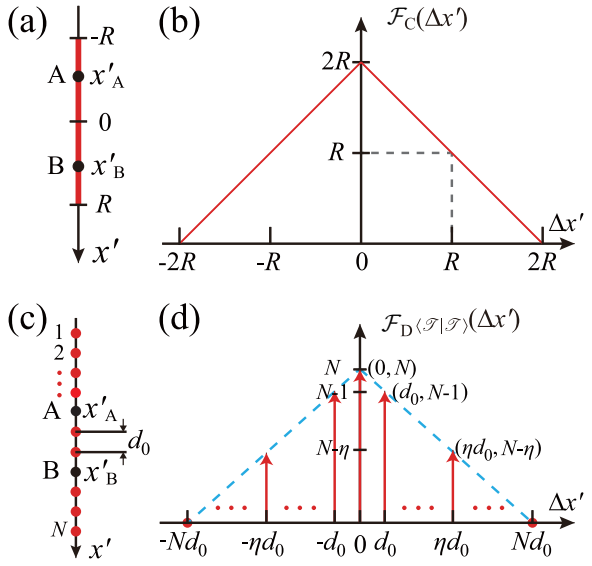

FIG. 2. (a) and (b) are the schematic diagrams of a 1D continuous chaotic light source with a size of $[-R, R]$ and its corresponding distribution density function $\mathcal{F}_C(\Delta x')$, respectively. (c) and (d) are the schematic diagrams of a typical 1D PDCLS $\mathscr{T}$ with a total number of point sources N and a period d_0 and its corresponding discrete distribution density function $\mathcal{F}_{D\langle\mathscr{T}|\mathscr{T}\rangle}(\Delta x')$, respectively.

amplitude distribution as shown in Fig. 2(a), there are many pairs of point light sources, each pair of them $\{x'_A, x'_B\}$ $(x'_A, x'_B \in [-R, R])$ will contribute a two-photon eigen mode with a specific eigen spatial frequency $\Delta x'/(\lambda z)$ $(\Delta x' \in [-2R, 2R])$. When two pairs of point light sources are of the same displacement $\Delta x'$, the resulting two-photon eigen modes are also the same because the eigen spatial frequency $\Delta x'/(\lambda z)$ is determined by the displacement $\Delta x'$. This means that each eigen mode is of different distribution density $\mathcal{F}_C(\Delta x')$, which can be written as

$$\mathcal{F}_C(\Delta x') = \int_{-R}^{R} \mathrm{rect}\left(\frac{\Delta x' - x'_A}{2R}\right)\mathrm{rect}\left(\frac{x'_A}{2R}\right)dx'_A = 2R\Lambda\left(\frac{\Delta x'}{2R}\right), \quad \text{with} \quad \Delta x' \in [-2R, 2R], \tag{3}$$

where the subscript C in $\mathcal{F}_C(\Delta x')$ denotes the case for the continuous chaotic light source, $\mathrm{rect}(x)$ is the rectangular function defined as $\mathrm{rect}(x) \equiv \begin{cases} 1, & |x| \leqslant \frac{1}{2} \\ 0, & \text{otherwise} \end{cases}$, and $\Lambda(x)$ is the triangle function defined as $\Lambda(x) \equiv \begin{cases} 1 - |x|, & |x| \leqslant 1 \\ 0, & \text{otherwise} \end{cases}$, as shown in Fig. 2(b).

The summation over all these weighted two-photon eigen modes will result in the second-order spatial correlation function of the continuous chaotic light source. For a continuous chaotic light source with a limited width $[-R, R]$, the second-order spatial correlation function on the far-field can then be calculated as

$$G_C^{(2)}(x_1, x_2) = \frac{1}{2}\int_{-2R}^{+2R} \mathcal{F}_C(\Delta x')G_{\mathrm{cross}}^{(2)}(x_1, x_2)d\Delta x' = I_0^2\mathrm{Re}\left[\overline{G}_C^{(2)}(x_1, x_2) + \widetilde{G}_C^{(2)}(x_1, x_2)\right], \tag{4}$$

where

$$\overline{G}_C^{(2)}(x_1, x_2) = \int_{-2R}^{+2R} \mathcal{F}_C(\Delta x')d\Delta x' = 4R^2 \tag{5}$$

and

$$\widetilde{G}_C^{(2)}(x_1, x_2) = \int_{-2R}^{+2R} \mathcal{F}_C(\Delta x')e^{-ik\Delta x'(x_1 - x_2)/z}d\Delta x' = 4R^2\mathrm{sinc}^2[2R(x_1 - x_2)/(\lambda z)]. \tag{6}$$

Here, the prefactor $\frac{1}{2}$ in Eq. (4) is due to the fact that the displacements $\Delta x'$ and $-\Delta x'$ are actually corresponding to exactly the same eigen mode. One may note that the self-correlation contribution is already included in Eq. (4) when $\Delta x' = 0$. On the right side of Eq. (4), the first term $\overline{G}_C^{(2)}(x_1, x_2)$ contributes a constant background, while the second term $\widetilde{G}_C^{(2)}(x_1, x_2)$ is the weighted superposition of two-photon eigen modes with continuous spectra, which is actually the Fourier transform of the distribution density function $\mathcal{F}_C(\Delta x')$. Note that all eigen modes are in phase at $x_1 - x_2 = 0$ but dephase gradually with the increase of $|x_1 - x_2|$, leading to the well-known HBT bunching effect of thermal light.

The normalized second-order spatial correlation function of the continuous chaotic light source can be calculated as [46,47]

$$g_C^{(2)}(x_1, x_2) = G_C^{(2)}(x_1, x_2)/(\langle I(x_1)\rangle\langle I(x_2)\rangle) = 1 + \mathrm{sinc}^2[2R(x_1 - x_2)/(\lambda z)], \tag{7}$$

where $\langle I(x_i)\rangle = 2RI_0$ $(i = 1, 2)$ is the ensemble averaged light intensity at position x_i on the detection plane and $\mathrm{sinc}(x) \equiv \sin(\pi x)/(\pi x)$, respectively. This conclusion is consistent with the result reported in the literature [36,37,42–45,48].

C. Discrete chaotic light sources

It is well known that in general the discrete system is of very different physical properties from the continuous system. Many novel optical phenomena have been reported for various discrete optical systems, such as Talbot effect [24] and Lau effect [25] in periodical discrete systems and the collapse and revival of the wave-packet evolution in quantum systems with discrete eigen wave functions [3]. Both the first-order and the second-order Talbot effects were reported, and all of them are in the Fresnel zone and in the longitudinal dimension [35]. Different from these temporal or longitudinal revival effects, here we will show that novel phenomena such as transverse revival and fractional revival of the HBT bunching effect can also be observed in the discrete chaotic light sources, which, however, is in the far-field (or the Fraunhofer zone) and in the transverse dimension.

1. Transverse revival of the HBT bunching effect

Supposing that there is a chain of discrete chaotic point light sources with equal distance between the nearest neighboring ones, where the point light sources are completely independent with respect to each other, forming a 1D periodical discrete chaotic light source (1D PDCLS), as shown in Fig. 2(c). Assuming that the total number of the point light sources in the 1D PDCLS is N, and the period of 1D

PDCLS is d_0. For convenience, we mark this set of 1D PDCLS as $\mathscr{T}$. Similarly, a pair of independent chaotic point light sources with a separation distance $\Delta x' = \eta d_0$ will contribute a discrete two-photon eigen mode with a specific eigen spatial frequency $\eta d_0/(\lambda z)$, where $\eta = -N, -N+1, \cdots, N-1, N$. The summation over all these discrete two-photon eigen modes results in the second-order spatial correlation function of the 1D PDCLS. For a specific 1D PDCLS with limited number of point sources N, the distribution density function of the discrete two-photon eigen modes is also discrete and can be expressed as

$$\mathcal{F}_{\mathrm{D}\langle\mathscr{T}|\mathscr{T}\rangle}(\Delta x') = N\Lambda\left(\frac{\Delta x'}{Nd_0}\right)\mathrm{one}\left(\frac{\Delta x'}{d_0}\right), \tag{8}$$

where the subscript D in $\mathcal{F}_{\mathrm{D}\langle\alpha|\beta\rangle}(\Delta x')$ indicates the case for the discrete chaotic light source, and the subscript $\langle\alpha|\beta\rangle$ indicates a set of pairs of point light sources contributing discrete eigen modes, in which, for each pair of point light sources, one point light source is from the set of discrete point light sources α, and the other one is from the set of discrete point light sources β; and the sampling function $\mathrm{one}(x)$ is equal to 1 for integers and 0 for all other values. In Eq. (8), both two discrete point light sources are from the same set $\mathscr{T}$. The distribution density function $\mathcal{F}_{\mathrm{D}\langle\mathscr{T}|\mathscr{T}\rangle}(\Delta x')$ of the 1D PDCLS is schematically illustrated in Fig. 2(d), where the blue dashed lines describe the envelope of the distribution density function $\mathcal{F}_{\mathrm{D}\langle\mathscr{T}|\mathscr{T}\rangle}(\Delta x')$, which in fact has the same profile as that of Eq. (3), as one can see from Figs. 2(b) and 2(d).

Consequently, the second-order spatial correlation function with the 1D PDCLS in the far-field can be written as

$$\begin{aligned} &G^{(2)}_{\mathrm{D}\langle\mathscr{T}|\mathscr{T}\rangle}(x_1, x_2) \\ &= \frac{1}{2}\sum_{\eta=-N}^{N}\mathcal{F}_{\mathrm{D}\langle\mathscr{T}|\mathscr{T}\rangle}(\eta d_0)G^{(2)}_{\mathrm{cross}}(x_1, x_2) \\ &= I_0^2\mathrm{Re}\big[\overline{G}^{(2)}_{\mathrm{D}\langle\mathscr{T}|\mathscr{T}\rangle}(x_1, x_2) + \widetilde{G}^{(2)}_{\mathrm{D}\langle\mathscr{T}|\mathscr{T}\rangle}(x_1, x_2)\big], \end{aligned} \tag{9}$$

where

$$\overline{G}^{(2)}_{\mathrm{D}\langle\mathscr{T}|\mathscr{T}\rangle}(x_1, x_2) = \sum_{\eta=-N}^{N}\mathcal{F}_{\mathrm{D}\langle\mathscr{T}|\mathscr{T}\rangle}(\eta d_0) = N^2 \tag{10}$$

and

$$\begin{aligned} \widetilde{G}^{(2)}_{\mathrm{D}\langle\mathscr{T}|\mathscr{T}\rangle}(x_1, x_2) &= \sum_{\eta=-N}^{N}\mathcal{F}_{\mathrm{D}\langle\mathscr{T}|\mathscr{T}\rangle}(\eta d_0)e^{-ik\eta d_0(x_1-x_2)/z} \\ &= \frac{\sin^2[\pi N d_0(x_1-x_2)/(\lambda z)]}{\sin^2[\pi d_0(x_1-x_2)/(\lambda z)]}. \end{aligned} \tag{11}$$

Again, the prefactor $\frac{1}{2}$ in Eq. (9) is due to the fact that every pair of point sources are counted for twice but only contribute one discrete two-photon eigen mode. The first term $\overline{G}^{(2)}_{\mathrm{D}\langle\mathscr{T}|\mathscr{T}\rangle}(x_1, x_2)$ on the right side of Eq. (9) is a constant background, while the second term $\widetilde{G}^{(2)}_{\mathrm{D}\langle\mathscr{T}|\mathscr{T}\rangle}(x_1, x_2)$ is the weighted superposition of a set of discrete two-photon eigen modes, which will result in the collapse and revival of the HBT bunching effect of the discrete chaotic light in the transverse dimension, as we will show below.

The normalized second-order spatial correlation function with the 1D PDCLS can then be expressed as

$$g^{(2)}_{\mathrm{D}\langle\mathscr{T}|\mathscr{T}\rangle}(x_1, x_2) = 1 + \frac{1}{N^2}\frac{\sin^2[\pi N d_0(x_1-x_2)/(\lambda z)]}{\sin^2[\pi d_0(x_1-x_2)/(\lambda z)]}. \tag{12}$$

One can see from Eq. (12) that the two-photon bunching behavior of the 1D PDCLS is completely different from that of the continuous chaotic light sources expressed by Eq. (7). In addition to the bunching peak at $x_1 - x_2 = 0$, which is the same as that with the continuous chaotic light source, the two-photon bunching peak can also be observed whenever the condition $\pi d_0|x_1 - x_2|/(\lambda z) = n\pi$ is satisfied, where $n = 0, 1, 2, \cdots$. This is understandable from Eqs. (9)–(11), as one can see that, it is the second term $\widetilde{G}^{(2)}_{\mathrm{D}}(x_1, x_2)$, i.e., the weighted superposition of a set of discrete two-photon eigen modes $e^{-ik\eta d_0(x_1-x_2)/z}$ ($\eta \in [-N, N]$), that results in the two-photon bunching effect of the 1D PDCLS. It is evident that all these discrete two-photon eigen modes are in phase at $x_1 - x_2 = 0$, leading to the traditional HBT bunching peak. With the increase of $|x_1 - x_2|$, these discrete two-photon eigen modes dephase and the bunching effect collapses. However, if $|x_1 - x_2|$ further increases up to $\lambda z/d_0$, then all these discrete two-photon eigen modes are in phase again, and the HBT bunching effect revives. The collapse and the revival of the HBT bunching effect repeat periodically along the transverse dimension in the detection plane. According to Eq. (12), the revival period of the HBT bunching effect T_{rev}, defined as the transverse distance between the nearest neighboring bunching peaks, is calculated to be $T_{\mathrm{rev}} = \lambda z/d_0$, and the bunching peak-to-background ratio is 2:1, the same as that of the continuous chaotic thermal light [36,37]. One may also note that there are $(N-1)$ minimal dips equal to 1 between two neighboring bunching peaks when $x_1 - x_2 = m\lambda z/(Nd_0)$ [$m = \pm1, \pm2, \cdots, \pm(N-1), \pm(N+1), \cdots$], and therefore there are $(N-2)$ submaximum between two neighboring bunching peaks. The half width of the main HBT bunching peak, defined as the transverse distance between the main peak position and its nearest first minimal position, can be calculated to be $W_{\mathrm{half}} = \lambda z/(Nd_0)$. The revival of the HBT bunching effect is a particular property for the discrete system, which can be referred to as the discrete HBT effect, no such revival can be observed with the continuous chaotic thermal light.

2. *Transverse fractional revival of the HBT bunching effect*

Now, let us make some modifications on the discrete chaotic point light source set $\mathscr{T}$. We take a set of chaotic point light source $\mathscr{E}$ out from $\mathscr{T}$. This set of chaotic point light source $\mathscr{E}$ is of equal distance between the nearest neighboring point light sources with a period of qd_0 ($q = 2, 3, \cdots$), and the position of the first chaotic point light source in $\mathscr{E}$ is at the ζth point light source in $\mathscr{T}$. The total number of the point light source in $\mathscr{E}$ is M, surely, we have $(M-1)q \leqslant (N-1)$. The remaining nonperiodic discrete chaotic light sources (non-PDCLS) form a set marked as $\mathscr{R}$, satisfying $\mathscr{T} = \mathscr{E} + \mathscr{R}$.

When one considers the second-order spatial correlation function of the discrete chaotic point light sources $\mathscr{R}$, the key is to find out all two-photon eigen modes originated from $\mathscr{R}$. According to the relationship $\mathscr{T} = \mathscr{E} + \mathscr{R}$, one has the

relationship for pairs of point light sources $\langle\mathscr{T}|\mathscr{T}\rangle = \langle\mathscr{R}|\mathscr{R}\rangle + \langle\mathscr{E}|\mathscr{E}\rangle + 2\langle\mathscr{R}|\mathscr{E}\rangle$ and $\langle\mathscr{T}|\mathscr{E}\rangle = \langle\mathscr{R}|\mathscr{E}\rangle + \langle\mathscr{E}|\mathscr{E}\rangle$. Thus, one has $\langle\mathscr{R}|\mathscr{R}\rangle = \langle\mathscr{T}|\mathscr{T}\rangle + \langle\mathscr{E}|\mathscr{E}\rangle - 2\langle\mathscr{T}|\mathscr{E}\rangle$, and the second-order spatial correlation function can be expressed as

$$G^{(2)}_{\mathrm{D}\langle\mathscr{R}|\mathscr{R}\rangle}(x_1,x_2) = I_0^2\mathrm{Re}\big[\overline{G}^{(2)}_{\mathrm{D}\langle\mathscr{R}|\mathscr{R}\rangle}(x_1,x_2) + \widetilde{G}^{(2)}_{\mathrm{D}\langle\mathscr{R}|\mathscr{R}\rangle}(x_1,x_2)\big], \tag{13}$$

where

$$\overline{G}^{(2)}_{\mathrm{D}\langle\mathscr{R}|\mathscr{R}\rangle}(x_1,x_2) = 2C^2_{N-M} + (N-M) = (N-M)^2, \tag{14}$$

and

$$\widetilde{G}^{(2)}_{\mathrm{D}\langle\mathscr{R}|\mathscr{R}\rangle}(x_1,x_2) = \widetilde{G}^{(2)}_{\mathrm{D}\langle\mathscr{T}|\mathscr{T}\rangle}(x_1,x_2) + \widetilde{G}^{(2)}_{\mathrm{D}\langle\mathscr{E}|\mathscr{E}\rangle}(x_1,x_2) - 2\widetilde{G}^{(2)}_{\mathrm{D}\langle\mathscr{T}|\mathscr{E}\rangle}(x_1,x_2). \tag{15}$$

According to the procedures in Sec. II C 1, one can easily obtain the first and the second terms in Eq. (15) because both $\mathscr{T}$ and $\mathscr{E}$ are 1D periodical discrete chaotic light sources with periods d_0 and qd_0, respectively, and they can be written as

$$\widetilde{G}^{(2)}_{\mathrm{D}\langle\mathscr{T}|\mathscr{T}\rangle}(x_1,x_2) = \frac{\sin^2[\pi N d_0(x_1-x_2)/(\lambda z)]}{\sin^2[\pi d_0(x_1-x_2)/(\lambda z)]}, \tag{16}$$

and

$$\widetilde{G}^{(2)}_{\mathrm{D}\langle\mathscr{E}|\mathscr{E}\rangle}(x_1,x_2) = \frac{\sin^2[\pi M q d_0(x_1-x_2)/(\lambda z)]}{\sin^2[\pi q d_0(x_1-x_2)/(\lambda z)]}. \tag{17}$$

The third term in Eq. (15) shows the superposition of two-photon eigen modes where the pairs of chaotic point light sources are from two different sets $\mathscr{T}$ and $\mathscr{E}$, respectively, and it can be calculated as

$$\widetilde{G}^{(2)}_{\mathrm{D}\langle\mathscr{T}|\mathscr{E}\rangle}(x_1,x_2) = \sum_{\chi=1}^{M}\sum_{\eta=1}^{N} e^{-ik\{\eta-[\zeta+(\chi-1)q]\}d_0(x_1-x_2)/z} = \gamma\frac{\sin\left[\frac{\pi M q d_0(x_1-x_2)}{\lambda z}\right]\sin\left[\frac{\pi N d_0(x_1-x_2)}{\lambda z}\right]}{\sin\left[\frac{\pi q d_0(x_1-x_2)}{\lambda z}\right]\sin\left[\frac{\pi d_0(x_1-x_2)}{\lambda z}\right]}, \tag{18}$$

where $\gamma = e^{-i2\pi L_{\langle\mathscr{T}|\mathscr{E}\rangle}(x_1-x_2)/(\lambda z)}$, in which $L_{\langle\mathscr{T}|\mathscr{E}\rangle} = [N+1-2\zeta-(M-1)q]d_0/2$ is the distance between the central positions of two point light source sets $\mathscr{T}$ and $\mathscr{E}$. Particularly, by setting $M=N$, $q=1$ and $\zeta=1$ in expression $\widetilde{G}^{(2)}_{\mathrm{D}\langle\mathscr{T}|\mathscr{E}\rangle}(x_1,x_2)$, it reduces to $\widetilde{G}^{(2)}_{\mathrm{D}\langle\mathscr{T}|\mathscr{T}\rangle}(x_1,x_2)$.

The normalized second-order spatial correlation function with the non-PDCLS $\mathscr{R}$ can then be written as

$$g^{(2)}_{\mathrm{D}\langle\mathscr{R}|\mathscr{R}\rangle}(x_1,x_2) = 1 + \frac{1}{(N-M)^2}\frac{\sin^2\left[\frac{\pi N d_0(x_1-x_2)}{\lambda z}\right]}{\sin^2\left[\frac{\pi d_0(x_1-x_2)}{\lambda z}\right]} + \frac{1}{(N-M)^2}\frac{\sin^2\left[\frac{\pi M q d_0(x_1-x_2)}{\lambda z}\right]}{\sin^2\left[\frac{\pi q d_0(x_1-x_2)}{\lambda z}\right]} - \frac{2\gamma_{Re}}{(N-M)^2}\frac{\sin\left[\frac{\pi M q d_0(x_1-x_2)}{\lambda z}\right]\sin\left[\frac{\pi N d_0(x_1-x_2)}{\lambda z}\right]}{\sin\left[\frac{\pi q d_0(x_1-x_2)}{\lambda z}\right]\sin\left[\frac{\pi d_0(x_1-x_2)}{\lambda z}\right]}, \tag{19}$$

where γ_{Re} is the real part of γ. One can see from Eqs. (15)–(19) that all discrete two-photon eigen modes are again in phase at $x_1-x_2=0$ but dephase gradually with the increase of $|x_1-x_2|$, resulting in a two-photon bunching peak of 2 at $x_1-x_2=0$. Similar to the case with the 1D PDCLS set $\mathscr{T}$, at the specific transverse positions $|x_1-x_2| = nT_{\mathrm{rev}}$ where $n=0,\ 1,\ 2,\ \cdots$, all two-photon eigen modes are in phase again and the two-photon bunching effect revives fully with a bunching peak-to-background ratio of 2, the same as that of the thermal light, as shown in Eq. (19). More interestingly, at the transverse positions $|x_1-x_2| = (n+\frac{p}{q})T_{\mathrm{rev}}$ where $p=1,\ 2,\ \cdots(q-1)$, the discrete two-photon eigen modes in Eqs. (16) and (18) are completely dephasing, and the superposition of them is exactly 0 when q is a factor of N. Even in the case when q is not a factor of N, these discrete two-photon eigen modes in Eqs. (16) and (18) are also dephasing, and their contribution to $g^{(2)}_{\mathrm{D}\langle\mathscr{R}|\mathscr{R}\rangle}(x_1,x_2)$ is negligibly small at $|x_1-x_2| = (n+\frac{p}{q})T_{\mathrm{rev}}$. This can be inferred from Eqs. (11) and (12). One knows that, for the discrete chaotic point light sources $\mathscr{T}$, the contribution of weighted superposition of discrete two-photon eigen modes to $g^{(2)}_{\mathrm{D}\langle\mathscr{T}|\mathscr{T}\rangle}(x_1,x_2)$ is negligibly small as compared to 1, so is the ratio $\frac{1}{N}\frac{\sin[\pi N d_0(x_1-x_2)/(\lambda z)]}{\sin[\pi d_0(x_1-x_2)/(\lambda z)]}$ at $|x_1-x_2| = (n+\frac{p}{q})T_{\mathrm{rev}}$. Note that $(N-M)$ is of the same order as N, therefore, the second term and the fourth term in Eq. (19) are also negligibly small at $|x_1-x_2| = (n+\frac{p}{q})T_{\mathrm{rev}}$ even when q is not a factor of N. However, the discrete two-photon eigen modes in Eq. (17) are always in phase at $|x_1-x_2| = (n+\frac{p}{q})T_{\mathrm{rev}}$ no matter q is a factor of N or not. The superposition of these in-phase two-photon eigen modes expressed by Eq. (17) leads to the partial revival, i.e., the fractional revival of the two-photon bunching effect with a bunching peak of $\sim 1+M^2/(N-M)^2$. This means that both transverse revival and fractional revival of the HBT bunching effects can be observed with the non-PDCLS $\mathscr{R}$.

3. Discussions

It should be noted that the bunching pattern of any chaotic light on the detection plane can also be derived from the Van Cittert-Zernike theorem [49,50], since the Van Cittert-Zernike theorem is applicable for any chaotic light source [51–54], including both continuous and discrete light sources. By employing the Van Cittert-Zernike theorem, the bunching pattern is explained as a result of the absolute-square of the Fourier transform of the intensity distribution of the chaotic light source. Therefore, for a periodic discrete point light source, its Fourier transform is also a periodic function. However, the underlying physics of the appearance of such periodic second-order correlation function, i.e., the revival of the HBT bunching effect, is not explicitly and clearly shown in the above Fourier transform way.

Here, we revealed explicitly the underlying physics for the formation of the periodic bunching pattern in the far-field detection plane, i.e., the revival of the HBT bunching effect is due to the in-phase superposition of all discrete two-photon eigen modes originated from the periodic discrete chaotic light sources, but not judged just by the value of $g^{(2)}(x_1,x_2)$. One notes that, it is the whole bunching curve, including both the central bunching peak and its side-lobe structure, that is revived periodically in the discrete chaotic light case. Such HBT bunching revival is specific for the discrete light source

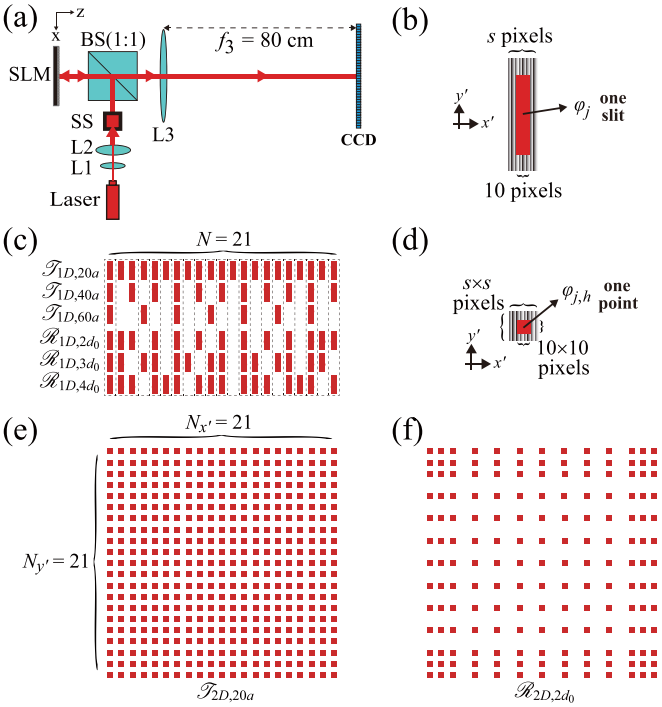

FIG. 3. (a) Schematic diagram of experimental setup to measure the HBT effects with discrete chaotic light sources. L1, L2, and L3: lenses; SS: square slot; BS: beam splitter; CCD: charge coupled device; SLM: spatial light modulator. (b), (d) The phase distribution within an elementary unit cell of 1D and 2D discrete chaotic light sources, respectively. The background phase structure was for a blazed grating, as indicated by the gray stripes. The 1D and 2D discrete chaotic sources were embedded on the background blazed grating, as indicated by the red areas where the random phase φ_j and $\varphi_{j,h}$ were encoded by the SLM on the jth and (j,h)th light sources in 1D and 2D discrete chaotic light sources, respectively. (c) The discrete arrays of the three 1D PDCLSs $\mathscr{T}_{1D,20a}$, $\mathscr{T}_{1D,40a}$ and $\mathscr{T}_{1D,60a}$, and the discrete arrays of the three 1D nonPDCLSs $\mathscr{R}_{1D,2d_0}$, $\mathscr{R}_{1D,3d_0}$ and $\mathscr{R}_{1D,4d_0}$, respectively. (e), (f) The discrete arrays of a 2D PDCLS $\mathscr{T}_{2D,20a}$ and a 2D nonPDCLS $\mathscr{R}_{2D,2d_0}$, respectively.

but not for the continuous light source, as one can see by comparing the results in Sec. II B and Secs. II C 1, II C 2.

It is known that the bunching curve profile can be modulated as reported by Strekalov *et al.* [54], where the width and the sidelobes of the bunching curve varied due to the presence of an absorptive object, through which the objective information such as the orientation of the object's transient trajectory can be inferred from the variance of the bunching curve profile. One notes that, such modulation on the profile of a specific bunching curve is conceptually different from the revival of the HBT bunching effect in which many identical bunching peaks will collapse and then revive periodically on the detection plane at different specific transverse positions.

III. EXPERIMENTAL VERIFICATION

Figure 3(a) shows the schematic diagram of the experimental setup to measure the second-order spatial correlation patterns of discrete chaotic light sources. In our experiments, a single-mode, continuous-wave laser beam operating at 780 nm was expanded and collimated by two lenses L1 and L2 and spatially reshaped by a square slot (SS) to generate a plane wave with a flat-top intensity distribution. This expanded and collimated flat-top light beam was reflected by a beam splitter (BS) with a 50:50 reflection/transmission ratio and then launched normally onto a reflection-type phase-only SLM (PLUTO 1080P from HOLOEYE Photonics AG, Germany, with an elementary square pixel of $a^2 = 8 \times 8\,\mu\text{m}^2$ and totally 1920 × 1080 pixels). The reflected beam from the SLM transmitted through the BS again and was then collected by a lens L3 with a focal length $f_3 = 80$ cm. The intensity distribution on the rear focal plane of the lens L3 (i.e., the far-field detection plane) was recorded by using a charge coupled device (CCD) camera, and totally 10 000 frames, each with a recording time of 1.0 ms, were measured and used to calculate the second-order correlation patterns on the detection plane.

Figure 3(b) shows the spatial distribution of the phase structure of an elementary unit cell in a typical 1D PDCLS. Here, we combined the neighboring s pixels of the SLM along the horizontal dimension [the x'-dimension in Fig. 3(b)] as an elementary unit cell, in which the central 10 pixels were loaded with the same random phase φ_j [see the red area in Fig. 3(b)] and served as the jth discrete slit sources, while the rest part of the elementary unit cell was loaded with the background phase structure working as the blazed grating [indicated by the gray stripes in Fig. 3(b)]. Note that, in the 1D PDCLS, the length-width ratio of each discrete slit source was much larger than 1 so that the phase can be effectively regarded to be uniform in the vertical dimension (i.e., the y'-dimension). In other words, as far as the phase distribution is considered, the discrete slit sources can be viewed as being embeded in the background 1D blazed grating. In this way, only the light beams reflected from the discrete slit sources were collected by the CCD on the detection plane [55]. One sees that the effective dimension size of each discrete slit source was $10a$, while the period of the 1D PDCLS d_0, i.e., the distance between the nearest neighboring discrete slit sources, was $s \times a$, respectively, in the x' dimension. For a given width D of the incident flat-top plane wave on the SLM, which was 3.35 mm in our experiment, the total number N of the discrete slit sources in the 1D PDCLS was equal to D/d_0. Here, we set the phase φ_j encoded on the jth discrete slit source of the 1D PDCLS being randomly and uniformly distributed within $[0, 2\pi)$. Note that, by replacing the phase φ_j with the surrounding phase required by the background blazed grating, the jth discrete slit source can be removed and a nonPDCLS can be conveniently designed. Based on the aforementioned technique, we designed three 1D PDCLSs and three 1D nonPDCLSs, respectively, as shown in Fig. 3(c). For the three PDCLSs, the periods were set to be $20a$, $40a$, and $60a$, and they were labeled as $\mathscr{T}_{1D,20a}$, $\mathscr{T}_{1D,40a}$, and $\mathscr{T}_{1D,60a}$, respectively. The corresponding total numbers N of the three 1D PDCLSs were therefore 21, 11, and 7, respectively. The three 1D nonPDCLSs were formed by removing slit source sets $\mathscr{E}_{1D}$ with different periods from the basic 1D PDCLS $\mathscr{T}_{1D,20a}$. The periods of the removed slit source sets $\mathscr{E}_{1D}$ were set to be $2d_0$, $3d_0$, and $4d_0$, respectively, with the corresponding first removed slit source being the 4th, 3rd, and 4th ones, respectively, as shown in Fig. 3(c). For convenience,

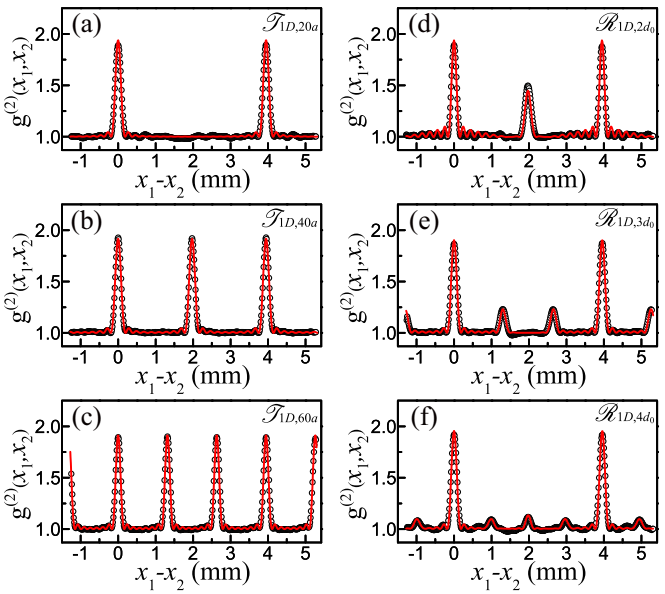

FIG. 4. Experimental observation of the transverse revival of the HBT bunching effect with the three 1D PDCLSs (a)–(c) and the transverse revival and fractional revival of the HBT bunching effect with the three 1D nonPDCLSs (d)–(f), respectively.

the remaining three 1D nonPDCLSs were marked as $\mathscr{R}_{1D,2d_0}$, $\mathscr{R}_{1D,3d_0}$, and $\mathscr{R}_{1D,4d_0}$, respectively, in the following.

The extension to the 2D cases is relatively simple. Figure 3(d) shows the spatial distribution of the phase structure of an elementary unit cell within the 2D PDCLS. Similarly, we combined the neighboring $s \times s$ pixels of the SLM as an elementary unit cell, within which the central 10×10 pixels were loaded with the same random phase $\varphi_{j,h}$ as those in the 1D PDCLS [see the red square in the inset of Fig. 3(d)], and the rest pixels were loaded with the phase required by the background blazed grating. The central 10×10 pixels with random phase $\varphi_{j,h}$, distributed with equal probability within $[0, 2\pi)$, served as the (j, h)th chaotic point source. Such unit cells repeated in both the x' and y' dimensions to form the 2D PDCLS, which can be viewed as being embedded in the background blazed grating. In our experiments, with an incident square flat-top plane wave of $D_{x'} \times D_{y'} = 3.35$ mm $\times$ 3.35 mm and $s = 20$, a 2D PDCLS $\mathscr{T}_{2D,20a}$ of a square array of 21×21 with an array period of $d_0 = 20a$ in both the x' and y' dimensions was produced, as shown in Fig. 3(e). By using the same technique as that in the 1D case, the corresponding 2D nonPDCLS can be produced by removing the corresponding periodic point source set $\mathscr{E}_{2D}$ from the 2D PDCLS $\mathscr{T}_{2D,20a}$, for example, by removing a 2D periodic point source array $\mathscr{E}_{2D,2d_0}$ with a period of $2d_0$ in both the x' and y' dimensions, as marked by $\mathscr{R}_{2D,2d_0}$ in Fig. 3(f).

Figure 4 shows the experimental results for the revival and the fractional revival of the bunching effect with both 1D PDCLSs and 1D nonPDCLSs, respectively. Note that the phases of the discrete chaotic sources were kept to be stationary when recording the intensity pattern for each frame, but the relative phases among the discrete chaotic sources in the array were random, and the phases of all discrete chaotic sources in the array changed randomly from one frame to the other. To calculate the second-order correlation patterns, totally 10 000 frames, each with an exposure time of 1.0 ms, were recorded for each second-order correlation pattern in Fig. 4. Here, the empty black circles in Fig. 4 are the experimental data, while the red curves are the corresponding theoretical fits. For the three 1D PDCLSs $\mathscr{T}_{1D,20a}$, $\mathscr{T}_{1D,40a}$, and $\mathscr{T}_{1D,60a}$, the measured second-order spatial correlation patterns are shown in Figs. 4(a)–4(c), respectively, in which the red curves are the theoretical fits by Eq. (12). One sees that the bunching effect collapses first and then revives periodically in the transverse x dimension. The revival periods of the bunching effects in Figs. 4(a)–4(c) were measured to be $T_{\text{rev}} = 3.95$ mm, 1.98 mm, and 1.32 mm, respectively, which are in good agreement with the theoretical prediction. The bunching peaks $g^{(2)}(x_1 - x_2 = nT_{\text{rev}})$ $(n = 0, \pm 1, \pm 2, \cdots)$ in Figs. 4(a)–4(c) were measured to be 1.94, 1.92, and 1.91, respectively, which is slightly lower than the theoretical limit 2 of the thermal chaotic light. This is mainly due to the facts that the random phase encoded on each discrete source was not perfectly random since the randomness was generated by computer and the phase encoded through SLM may slightly deviate from the designed ideal values because the SLM's phase encoding linearity may not be perfect. In addition, the half width of bunching peaks in Figs. 4(a)–4(c) were measured to be $W_{\text{half}} =$ 191 μm, 197 μm, and 178 μm, respectively, which are also consistent with the theoretical value $f_3\lambda/(Nd_0) = 186$ μm.

For the three 1D nonPDCLSs $\mathscr{R}_{1D,2d_0}$, $\mathscr{R}_{1D,3d_0}$, and $\mathscr{R}_{1D,4d_0}$, the measured second-order spatial correlation patterns are shown in Figs. 4(d)–4(f), respectively. Again, the empty black circles are the experimental data and the red solid curves are the theoretical fits by using Eq. (19). One sees that, in addition to the revival bunching peaks at $|x_1 - x_2| = nT_{\text{rev}}$ where $n = 0, 1, 2, \cdots$, the fractional revival bunching peaks were also observed at the appropriate transverse positions. For example, for the 1D nonPDCLS $\mathscr{R}_{1D,2d_0}$, the bunching effect partially revives at $|x_1 - x_2| = (n + \frac{1}{2})T_{\text{rev}}$ with a fractional bunching peak of $\sim$1.50, as shown in Fig. 4(d). Similarly, for the 1D nonPDCLS $\mathscr{R}_{1D,3d_0}$, the fractional revival bunching effect can be observed at $|x_1 - x_2| = (n + \frac{1}{3})T_{\text{rev}}$ and $(n + \frac{2}{3})T_{\text{rev}}$ with a fractional bunching peak of $\sim$1.23, while for the 1D nonPDCLS $\mathscr{R}_{1D,4d_0}$, the fractional revival bunching effect can be observed at $|x_1 - x_2| = (n + \frac{1}{4})T_{\text{rev}}$, $(n + \frac{2}{4})T_{\text{rev}}$ and $(n + \frac{3}{4})T_{\text{rev}}$ with a fractional bunching peak of $\sim$1.10, respectively, as shown in Figs. 4(e) and 4(f), respectively. Again, here $n = 0, 1, 2, \cdots$. These fractional revival bunching observations are in good accordance with the theoretically predicted ones, which are calculated to be 1.50, 1.26, and 1.12, respectively, for the 1D nonPDCLSs $\mathscr{R}_{1D,2d_0}$, $\mathscr{R}_{1D,3d_0}$, and $\mathscr{R}_{1D,4d_0}$ by using Eq. (19).

Figure 5 depicts the revival and the fractional revival of the HBT bunching effect with 2D PDCLS $\mathscr{T}_{2D,20a}$ and 2D nonPDCLS $\mathscr{R}_{2D,2d_0}$, respectively. Similarly, for the 2D PDCLS $\mathscr{T}_{2D,20a}$, the bunching effect collapses first and then revives periodically in both the transverse x and y dimensions with a period of $T_{\text{rev}} = 3.95$ mm and a half width of the bunching peaks $W_{\text{half}} \sim 188$ μm. While for the 2D nonPDCLS $\mathscr{R}_{2D,2d_0}$ with a characteristic removed point source array $\mathscr{E}_{2D,2d_0}$ of a period of $2d_0$ in both the x' and y' dimensions, as shown in Fig. 3(f), in addition to the revival bunching peaks at

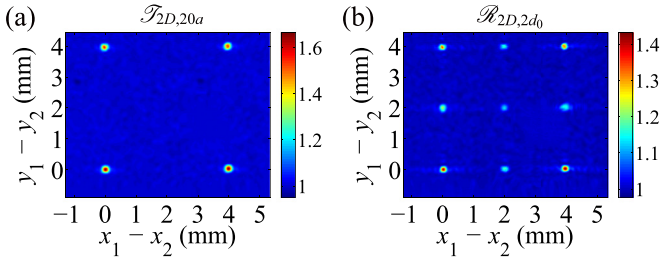

FIG. 5. Experimental results of the HBT bunching revivals with the 2D PDCLS $\mathscr{T}_{2D,20a}$ (a), and the revival and the fractional revival of the HBT bunching effect with the 2D nonPDCLS $\mathscr{R}_{2D,2d_0}$ (b), respectively.

$(|x_1 - x_2|, |y_1 - y_2|) = (nT_{\rm rev}, mT_{\rm rev})$, the fractional revival peaks appear at $(|x_1 - x_2|, |y_1 - y_2|) = [(n + \frac{1}{2})T_{\rm rev}, (m + \frac{1}{2})T_{\rm rev}]$, where $n, m = 0, 1, 2, \cdots$. As expected, the fractional revival peaks are lower than the revival peaks in general, which are in good agreement with the theoretical predictions.

IV. GHOST IMAGING COPY

One of the important applications of the HBT bunching effect is the ghost imaging, in which the bunching effect builds up the one-to-one point correlation between the object and the image planes [47,56–59]. It is evident that the transverse revival and fractional revival of the HBT bunching effects build up a deterministic one-to-multiple point correlation between the object and the image planes, therefore, this provides a possibility to copy the ghost image in the transverse dimension based on the HBT bunching revival and fractional revival of the discrete chaotic light.

Figure 6 shows the schematic diagram of the experimental setup to copy the ghost image in the transverse dimensions with a 2D discrete chaotic light source. The setup was built after that in Fig. 3(a) by adding a $2f$–$2f$-imaging system with lens L4 after the rear focal plane of lens L3 in Fig. 3(a). The discrete chaotic light sources $\mathscr{T}_{2D,20a}$ and $\mathscr{R}_{2D,2d_0}$ were employed, respectively, and the focal length of lens L4 was set to be 5.1 cm in the experiment. We put an amplitude transmitting double-slit with a slit width of 200 μm and a separation distance between two transmitting slits of 400 μm on the left-bottom corner of the input object plane of the $2f$–$2f$-imaging system (i.e., the rear focal plane of lens L3) as

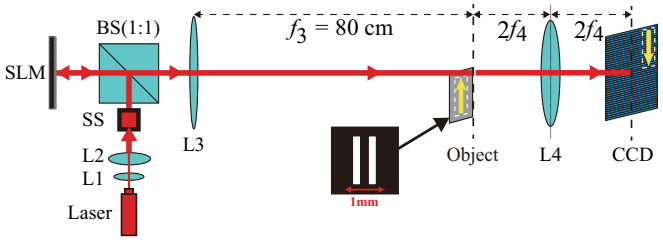

FIG. 6. Experimental setup for the ghost imaging copy with a 2D discrete chaotic light source. A $2f$–$2f$-imaging system with lens L4 of a focal length 5.1 cm was added after the setup shown in Fig. 3(a). A double-slit was served as an input object, placing at the left-bottom corner of the object plane of the $2f$–$2f$-imaging system.

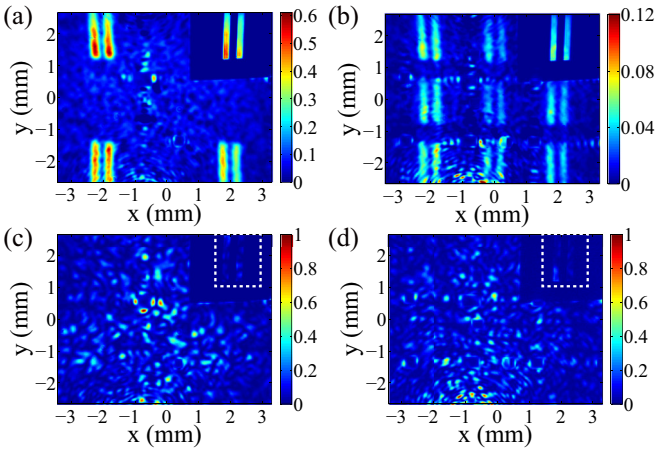

FIG. 7. (a) and (b) are the measured ghost imaging copies with the 2D PDCLS $\mathscr{T}_{2D,20a}$ and the 2D nonPDCLS $\mathscr{R}_{2D,2d_0}$, respectively. (c) and (d) depict the typical intensity distribution of a single frame with the 2D PDCLS $\mathscr{T}_{2D,20a}$ and the 2D nonPDCLS $\mathscr{R}_{2D,2d_0}$, respectively. The white dashed rectangles in (c) and (d) are the integral areas used to calculate the total transmitting intensity through the double-slit BI_i.

the object, and then recorded the intensity distribution on the image plane of the $2f$–$2f$-imaging system by a CCD camera. To obtain the ghost image, 10 000 frames of the intensity distribution were recorded, each with an exposure time of 1.0 ms. The ghost image $\mathcal{I}_{\rm ghost}(x, y)$ on the image plane of the $2f$–$2f$-imaging system can be calculated through [60,61]

$$\mathcal{I}_{\rm ghost}(x, y) = \frac{1}{10\,000} \sum_{i=1}^{10\,000} (BI_i - \langle BI \rangle) I_i(x, y), \tag{20}$$

where $I_i(x, y)$ is the intensity distribution of the ith frame, BI_i is the total transmitting intensity through the double-slit of the ith frame, and $\langle BI \rangle$ is the ensemble average over all measured BI_i.

Figures 7(a) and 7(b) show the experimentally measured ghost images with 2D PDCLS $\mathscr{T}_{2D,20a}$ and 2D nonPDCLS $\mathscr{R}_{2D,2d_0}$, respectively. In comparison, we also give the corresponding typical intensity distribution of a single frame $I_i(x, y)$, as shown in Figs. 7(c) and 7(d), respectively. Here, BI_i was obtained through an intensity integration over the area within the white dashed rectangle on the right-top corner of Fig. 7(c) or 7(d), which was the total transmitting intensity through the double-slit, equivalent to the case detected by a bucket detector without spatial resolution. One sees that, in addition to the self-correlated ghost image at the right-top corner of the image plane, there are many ghost image copies right at the HBT bunching revival and fractional revival positions in Figs. 7(a) and 7(b) with 2D PDCLS $\mathscr{T}_{2D,20a}$ and 2D nonPDCLS $\mathscr{R}_{2D,2d_0}$, respectively. Correlation-imaging in the transverse dimension was also observed based on the self-similarity of the periodical diffraction pattern from the periodical pinhole arrays [62,63]. In contrast, for the conventional intensity imaging, except for the conventional image at the right-top corner of the image plane, the rest area on the image plane is distributed with mussily speckled light spots and no image can be observed, as shown in Figs. 7(c) and 7(d).

One notes that the imaging technique here is also different from the one employed by Strekalov *et al.* [54], where the object information was obtained through the measurement of the width variation of the bunching curve combined with the intensity measurement. In our case, as shown in Fig. 6, although the illumination light is a discrete chaotic light, but the light field on the object plane is spatially intensity correlated due to the HBT bunching revival effect, therefore, one can achieve ghost image copy in the transverse dimension on the imaging plane, and many ghost images appear on the imaging plane, as shown in Fig. 7.

V. CONCLUSION

In conclusion, we proposed theoretically and demonstrated experimentally the transverse integer and fractional HBT bunching revivals of discrete chaotic light sources, which are the results of in-phase constructive interference of multiple discrete two-photon eigen modes of the discrete chaotic light sources. It is seen that the discrete HBT bunching effect with discrete chaotic light sources is very different from the traditional HBT bunching effect with the spatially continuous chaotic light sources. The HBT bunching effect collapses first and then revives fully and periodically in the transverse dimension of the far-field detection plane with periodical discrete chaotic light sources. The fractional HBT bunching revival, which is due to the in-phase superposition of parts of two-photon eigen modes, occurs with the nonperiodical discrete chaotic light sources which is formed when a set of discrete periodical chaotic light source with a q-multiple fundamental periodicity qd_0 is removed from the original fundamental periodical discrete chaotic light sources with a fundamental period of d_0. No revival and fractional revival can be observed with spatially continuous chaotic light. Both the integer and fractional HBT bunching revivals were confirmed experimentally with 1D and 2D discrete chaotic light sources. Possible applications such as ghost image copy were also proposed and demonstrated experimentally.

ACKNOWLEDGMENTS

This work is financially supported by the National Natural Science Foundation of China (NSFC) (Grants No. 91750204, No. 11774182, and No. 11604150); the 111 project (Grant No. B07013); and the Fundamental Research Funds for the Central Universities.

[1] H. Poincaré, Acta Math. **13**, 5 (1890).
[2] P. Bocchieri and A. Loinger, Phys. Rev. **107**, 337 (1957).
[3] R. W. Robinett, Phys. Rep. **392**, 1 (2004).
[4] C. U. Segre and J. D. Sullivan, Am. J. Phys. **44**, 729 (1976).
[5] R. Bluhm, V. A. Kostelecký, and J. A. Porter, Am. J. Phys. **64**, 944 (1996).
[6] D. L. Aronstein and C. R. Stroud, Jr., Phys. Rev. A **55**, 4526 (1997).
[7] B. R. Holstein, Am. J. Phys. **66**, 583 (1998).
[8] D. F. Styer, Am. J. Phys. **58**, 742 (1990).
[9] K. R. Naqvi and S. Waldenstrøm, Phys. Scr. **62**, 12 (2000).
[10] G. Alber, H. Ritsch, and P. Zoller, Phy. Rev. A **34**, 1058 (1986).
[11] J. Parker and C. R. Stroud, Jr., Phys. Rev. Lett. **56**, 716 (1986).
[12] J. A. Yeazell, M. Mallalieu, and C. R. Stroud, Jr., Phys. Rev. Lett. **64**, 2007 (1990).
[13] F. W. Cummings, Phys. Rev. **140**, A1051 (1965).
[14] J. H. Eberly, N. B. Narozhny, and J. J. Sanchez-Mondragon, Phys. Rev. Lett. **44**, 1323 (1980).
[15] N. B. Narozhny, J. J. Sanchez-Mondragon, and J. H. Eberly, Phys. Rev. A **23**, 236 (1981).
[16] Y. Kaluzny, P. Goy, M. Gross, J. M. Raimond, and S. Haroche, Phys. Rev. Lett. **51**, 1175 (1983).
[17] G. Rempe, H. Walther, and N. Klein, Phys. Rev. Lett. **58**, 353 (1987).
[18] M. Herrera, T. M. Antonsen, E. Ott, and S. Fishman, Phys. Rev. A **86**, 023613 (2012).
[19] E. M. Wright, D. F. Walls, and J. C. Garrison, Phys. Rev. Lett. **77**, 2158 (1996).
[20] G. Raithel, W. D. Phillips, and S. L. Rolston, Phys. Rev. Lett. **81**, 3615 (1998).
[21] A. S. Parkins and D. F. Walls, Phys. Reports **303**, 1 (1998).
[22] M. Greiner, O. Mandel, T. W. Hänsch, and I. Bloch, Nature **419**, 51 (2002).
[23] I. S. Averbukh and N. F. Perelman, Phys. Lett. A **139**, 449 (1989).
[24] H. F. Talbot, The London, Edinburgh, Dublin Philos. Mag. J. Sci. Ser 3 **9**, 401 (1836).
[25] E. Lau, Ann. Phy. **437**, 417 (1948).
[26] O. Bryngdahl, J. Opt. Soc. Am. **63**, 416 (1973).
[27] R. Iwanow, D. A. May-Arrioja, D. N. Christodoulides, G. I. Stegeman, Y. Min, and W. Sohler, Phys. Rev. Lett. **95**, 053902 (2005).
[28] K.-H. Luo, J. Wen, X.-H. Chen, Q. Liu, M. Xiao, and L.-A. Wu, Phys. Rev. A **80**, 043820 (2009).
[29] Y. Zhang, J. Wen, S. N. Zhu, and M. Xiao, Phys. Rev. Lett. **104**, 183901 (2010).
[30] J.-S. Xu, C.-F. Li, M. Gong, X.-B. Zou, C.-H. Shi, G. Chen, and G.-C. Guo, Phys. Rev. Lett. **104**, 100502 (2010).
[31] V. Torres-Company, J. Lancis, H. Lajunen, and A. T. Friberg, Phys. Rev. A **84**, 033830 (2011).
[32] L. Rayleigh, London, Edinburgh, Dublin Philos. Mag. J. Sci. Ser 5 **11**, 196 (1881).
[33] K. Patorski, *The Self-Imaging Phenomenon and Its Applications*, in *Progress in Optics*, edited by E. Wolf (North-Holland, Amsterdam, 1989), Vol. 27, pp. 1–108.
[34] J. M. Cowley, *Diffraction Physics*, 3rd ed. (Elsevier, Amsterdam, 1995).
[35] J. Wen, Y. Zhang, and M. Xiao, Adv. Opt. Photonics **5**, 83 (2013).
[36] R. H. Brown and R. Q. Twiss, Nature **177**, 27 (1956).
[37] R. H. Brown and R. Q. Twiss, Nature **178**, 1046 (1956).
[38] C. H. Raymond Ooi and B. L. Lan, Phys. Rev. A **81**, 063832 (2010).
[39] X.-B. Song, H.-B. Wang, J. Xiong, K. Wang, X. Zhang, K.-H. Luo, and L.-A. Wu, Phys. Rev. Lett. **107**, 033902 (2011).
[40] K.-H. Luo, X.-H. Chen, Q. Liu, and L.-A. Wu, Phys. Rev. A **82**, 033803 (2010).

[41] X.-B. Song, J. Xiong, X. Zhang, and K. Wang, Phys. Rev. A **82**, 033823 (2010).
[42] U. Fano, Am. J. Phys. **29**, 539 (1961).
[43] L. Mandel and E. Wolf, Rev. Mod. Phys. **37**, 231 (1965).
[44] H. Paul, Rev. Mod. Phys. **58**, 209 (1986).
[45] L. Mandel, Rev. Mod. Phys. **71**, S274 (1999).
[46] M. O. Scully and M. S. Zubairy, *Quantum Optics* (Cambridge University Press, Cambridge, 1997).
[47] Y. Shih, *An Introduction to Quantum Optics: Photon and Biphoton Physics* (CRC Press, Boca Raton, FL, 2011).
[48] P. Hong, L. Li, J. Liu, and G. Zhang, Sci. Rep. **6**, 23614 (2016).
[49] P. H. Van Cittert, Physica **1**, 201 (1934).
[50] F. Zernike, Physica **5**, 785 (1938).
[51] J. Cheng and S. Han, Phys. Rev. Lett. **92**, 093903 (2004).
[52] R. Cerbino, Phys. Rev. A **75**, 053815 (2007).
[53] A. S. Ostrovsky, G. Martínez-Niconoff, P. Martínez-Vara, and M. A. Olvera-Santamaría, Opt. Express **17**, 1746 (2009).
[54] D. V. Strekalov, B. I. Erkmen, and N. Yu, Phys. Rev. A **88**, 053837 (2013).
[55] G. Brooker, *Modern Classical Optics* (Oxford University Press, Oxford, 2003).
[56] D. V. Strekalov, A. V. Sergienko, D. N. Klyshko, and Y. H. Shih, Phys. Rev. Lett. **74**, 3600 (1995).
[57] T. B. Pittman, Y. H. Shih, D. V. Strekalov, and A. V. Sergienko, Phys. Rev. A **52**, R3429 (1995).
[58] B. Sun, M. P. Edgar, R. Bowman, L. E. Vittert, S. Welsh, A. Bowman, and M. J. Padgett, Science **340**, 844 (2013).
[59] M. Padgett, R. Aspden, G. Gibson, M. Edgar, and G. Spalding, Opt. Photon. News **27**, 38 (2016).
[60] O. Katz, Y. Bromberg, and Y. Silberberg, Appl. Phys. Lett. **95**, 131110 (2009).
[61] F. Ferri, D. Magatti, A. Gatti, M. Bache, E. Brambilla, and L. A. Lugiato, Phys. Rev. Lett. **94**, 183602 (2005).
[62] H. Li, Z. Chen, J. Xiong, and G. Zeng, Opt. Express **20**, 2956 (2012).
[63] H. Li, J. Shi, Y. Zhu, and G. Zeng, Appl. Phys. Lett. **103**, 051901 (2013).